PCCP

Accepted Manuscript

ROYAL SOCIETY OF CHEMISTRY

www.rsc.org/pccp

Journal Name

RSCPublishing

ARTICLE

Full-Printable Transparent Monolithic Solid-state Dye-Sensitized Solar Cell with Mesoscopic Indium Tin Oxide Counter Electrode

Cite this: DOI: 10.1039/xoxxooooox

Received ooth January 2012,
Accepted ooth January 2012

DOI: 10.1039/xoxxooooox

www.rsc.org/

Ying Yang, Kwangho Ri, Yaoguang Rong, Linfeng Liu, Tongfa Liu, Min Hu, Xiong Li, Hongwei Han*

We present a new transparent monolithic mesoscopic solid-state dye-sensitized solar cell employing trilamellar films of mesoscopic TiO_2 nanocrystalline photoanode, ZrO_2 insulating layer and Indium Tin Oxide counter electrode (ITO-CE) by screen-printing technology layer by layer. When the thickness of the ITO-CE was optimized to 2.1 um, this very simple and full printable solid-state DSSC with D102 dye and spiro-OMeTAD hole transport materials presents efficiencies of 1.73% irradiated from the front side and 1.06% irradiated from the rear side under a standard simulated sunlight condition (AM1.5 Global, 100mW/cm^2). Higher parameters could be expected with better transparent mesoscopic counter electrode and hole conductor for the printable monolithic mesoscopic solid-state DSSC.

Introduction

Since being reported by B. O'Regan and M. Grätzel in 1991, dye-sensitized solar cell (DSSC) has attracted much attention for its low cost, simple process and short energy payback times[1-3]. Meanwhile, building integrated photovoltaic (BIPV) with translucent power windows and roofs is regarded as one of method assembling construction esthetics and cost reduction of photovoltaic cells, thereby the transparent bifacial DSSC has increasingly fostered scientific and industrial research especially on the transparent counter electrode (CE) such as Pt, Graphene[4], Graphene Nano-platelets[5], Graphene/PEDOT-PSS[6], NiS[7], PANI[8], PEDOT[9] and so on. However, all of these strategies are focused on the conventional sandwich structure DSSC based on two transparent conducting glasses, which still suffering from leakage, corrosion and long-term stability problems of the liquid-state electrolytes in practical application. Normally, these issues could be avoided by replacing the liquid electrolyte with solid-state intermedium such as organic [10-12] or inorganic[13, 14] hole transporting materials (HTM). Since being reported by U. Bach et al. in 1998[11], the amorphous organic material spiro-OMeTAD (2,2′,7,7′-tetrakis-(N,N′-di-p-meth-oxy-phenylamine)-9,9′-spirobifluorene) has been considered as the most promising HTM for solid-state DSSCs, due to its high glass transition temperature, high solubility and proper absorption spectrum.[15] However, there are few reports on the transparent monolithic solid-state DSSCs with the spiro-OMeTAD and the transparent counter electrode. Despite the Pt electrode could be prepared by depositing a thin layer, a main problem that always encountered is its high reflectance[16]. For graphene, PANI and PEDOT organic materials based counter electrodes, the thickness is required to be up to several micrometers to obtain desired conductivity, [17, 18] which makes it difficult to be transparent. Interested, in 2012 Y. F. Chiang et al. reported a solid-state DSSC based on a transparent tin doped indium oxide (ITO) film CE through sputtering technology and obtained efficiency of 1.96% from photoanode side illumination and 1.50% from ITO side illumination[19]. In order to prevent the organic layer being damaged during the sputtering process, an Au thin film was deposited between spiro-OMeTAD and ITO film CE. Obviously, the sputtering technology is not only a complicated and high energy consuming process, but the usage of Au will further increases the material cost and reduce the transmittance of the device. Indeed, there is still an issue to find a high quality and reproducible transparent CE toward low-cost for the transparent solid-state DSSC.

Herein we firstly employed a transparent mesoscopic ITO CE (ITO-CE) to assemble a bifacial transparent monolithic solid-state DSSC. The revolutionary design is that the TiO_2 photoanode, the ZrO_2 insulating layer and the ITO-CE could be screen-printed layer by layer on a single substrate such as fluorine-doped tine oxide (FTO) glass, and then sensitized with the dye such as D102 and filling with the hole transport materials such as spiro-OMeTAD. Obviously, this design avoids the damage of sputtering process on the spiro-OMeTAD surface and offers an enhanced contact between the hole

transport material and CE for the using of mesoscopic structure with large surface-area. As a result, efficiencies of 1.73% from FTO side illumination and 1.06% from ITO side illumination were obtained within the transparent monolithic solid-state DSSC.

Experimental

ITO nanoparticles were synthetized by a simple solvothermal method. 36ml $InCl_3 \cdot 4H_2O$ (4.981g, 0.02mol) ethylene glycol solution, 4ml $SnCl_4$ (0.521g, 0.002mol) ethylene glycol solution and 40ml NaOH (3.2g, 0.08mol) ethylene glycol solution were mixed together and agitated at 0℃. Then the suspension was transported into a 250ml Teflon-lined autoclave and aged at 250℃for 24 hours.

The ITO nanoparticles were washed and centrifugal separated for 3 times respectively with water and ethanol. Then ITO nanoparticles, hydroxypropyl cellulose (Sigma) and terpineol (Sigma) were mixed in an agate jar and the mixture was stirred vigorously via ball milling for 2 h. The mass ratio of ITO: cellulose: terpineol was controlled to 1: 0.3: 5.

Typical monolithic solid-state DSSCs were fabricated as following: FTO glass substrates were etched with laser and cleaned ultrasonically for 10 minutes with detergent, deionized water and ethanol successively. FTO glass plates with high transparency in the visible range purchased from CSG Holding Co. LTD. A compact TiO_2 layer was deposited on the patterned FTO substrate by spray pyrolysis, after the temperature cooled down to room temperature, a TiO_2 layer was printed on the compact TiO_2 layer and then dried for 10 min at 70 °C to remove the solvent in the layer. After that the ZrO_2 layer printed on the TiO_2 layer and then dried for 10 min at 70 °C. Finally the ITO layer was printed on the ZrO_2 layer and then were gradually heated to 325 °C at a speed of 10°C/min and kept for 5 min, to 375 °C at a speed of 7.5°C/min and kept for 5 min, to 450 °C at a speed of 5°C/min and kept for 15 min, and finally, to 500 °C at a speed of 5°C/min and kept for 30 min. After the temperature reduced to 80℃, the device was immersed into D102 solution (0.5mM in CH_3CN: t-BuOH (1:1)) for 12 hours. Finally, the spiro-OMeTAD HTM solution was dropped into the ITO layer and heated at 50℃ until they dried. The spiro-OMeTAD solution was obtained as follows: Spiro-OMeTAD was dissolved in chlorobenzene at a concentration of 0.15 M, and then 0.021 M LiTFSI and 0.12 M TBP were added.

The sheet resistance of the films composed with ITO nanoparticles after sintering was carried out with a four-point probe detector (KDY-1, Guangzhou Kunde Ltd.). The thickness of the film was measured with a profilometer (Veeco Dektak 150). The X-ray Diffraction (XRD) spectra was used a D8 advance X-ray diffractor-meter with Ca-Ka radiation (k=1.5418). The structure of monolithic solid-state DSSC was observed using scanning electron microscopy (Nova NanoSEM450). The high-resolution transmission electron microscopy (TEM) pattern was tested by Tecnai G2-20 Twin. Electrochemical impedance spectroscopy (EIS) of the cell was carried on a potentiostat (EG&G, M2273) under dark condition and processed with Zview software. Photocurrent density–voltage characteristics were measured with a Keithley 2400 source meter under illumination with an Oriel solar simulator composed of a 1000 W xenon arc lamp and AM 1.5 G filters. The illuminated active area was obtained with a black mask containing a circular hole of $0.13cm^2$. The incident photon conversion efficiency was measured with a QE/IPCE Measurement Kit system (Newport, USA).

Results and discussion

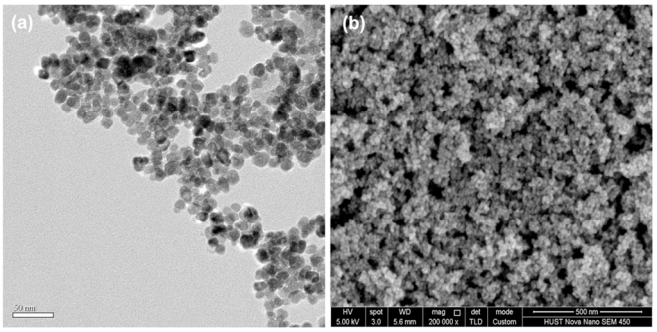

Figure 1 a) Transmission electron microscope (TEM) image of ITO nanoparticles and b) scanning electron microscopy (SEM) image of mesoscopic ITO film prepared by screen-printing technology.

The X-ray diffraction (XRD) pattern of the film composed with ITO nanoparticles deposited on glass substrate is showed in **Figure S1**. The peaks at 21.58°, 30.58°, 35.54°, 37.45°, 42.02°, 45.86°, 51.12°, 55.94° and 60.84° corresponding to (211), (222), (400), (411), (332), (431), (440), (611) and (622) obviously indicate that the ITO nanocrystals in the films are simple cubic structure. With Scherer's Equation, the average diameter of the ITO nanoparticles is 18.8 nm calculated from the broadening of the (222) XRD peak. This could also be confirmed by the Transmission Electron Microscope (TEM) image of the ITO nanoparticles as shown in **Figure 1a**. It could be found that in TEM image most of the ITO nanoparticles are cubic structure and the average size of the nanoparticles is around 19 nm, which is in accordance with the diameter calculated by XRD results. The surface pattern of the transparent mesoscopic conductive ITO film presented in **Figure 1b** exhibits characteristic of multi-pores in mesoscopic film, which was obtained after sintering at 500℃ for 30mins. The mesoscopic film favors the dye (D102) to pass through ITO-CE and to be adsorbed onto TiO_2 surface. At the same time, Spiro-OMeTAD HTM could penetrate into the mesoscopic pores of TiO_2 and ZrO_2 layers. Such cubic-shaped ITO nanoparticles might be expected to show lower interfacial resistance than uncontrolled particles due to larger contact area between the cubic-shaped nanoparticles, which reduced the interfacial resistance.[20] In this case the sheet resistance $R_{\square}$ of the transparent mesoscopic conductive ITO film was measured with a four-point probe detector and the thickness of the film was characterized with a

profilometer, indicating the electrical resistivity ρ is low to 0.247±0.004 Ω·cm.

Figure 2a shows the schematic structure of a bifacial transparent mesoscopic solid-state DSSC with the ITO-CE. A compact TiO_2 layer was deposited on the FTO substrate by a spray pyrolysis method and a TiO_2 mesoscopic layer, a ZrO_2 insulating layer and an ITO-CE layer were screen-printed layer by layer on the compact TiO_2 layer orderly. After the triple-layers were sintered at 500 °C for 30 min, the ethyl cellulose was removed and then the pores in the multi-layers were formed and combined to interconnected channels structure. Then the Spiro-OMeTAD HTM solution penetrated through the channels and filled the pores in the multi-layers. **Figure 2b** illustrates the SEM cross-sectional image of the solid-state DSSC with an ITO-CE, in which an optimized ~2.1 um ITO layer, a ~2.2 um TiO_2 layer and a ~1.5 um ZrO_2 layer[15, 21] are observed.

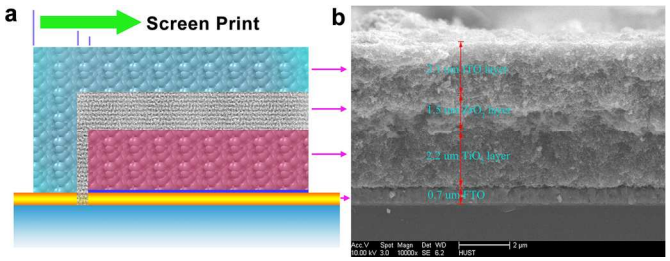

Figure 2 a) The schematic structure of a bifacial transparent monolithic solid-state DSSC with ITO-CE and b) Cross-sectional SEM image of the bifacial transparent solid-state DSSC based on ITO-CE.

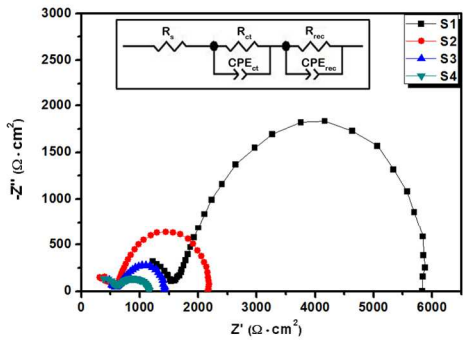

Figure 3 Nyquist plots of the solid-state DSSCs based on ITO-CEs with different thickness. Inserting picture is the equivalent circuit.

Table 1 Parameters obtained from the electric impedance spectra (EIS) of the solid-state DSSCs based on ITO-CE with the thickness of 1.1um (S1), 2.1um (S2), 3.1um (S3) and 4.0 um (S4).

Sample	R_s (Ω·cm^2)	Rct (Ω·cm^2)	Rrec (Ω·cm^2)
S1	755	860	4401
S2	227	557	1559
S3	216	420	712
S4	287	317	547

The power conversion efficiency of solid-state DSSC heavily relies on its series resistance R_s, charge transfer resistance R_{ct} and recombination resistance R_{rec}, which is related to the HTM filling fraction and $R_{□}$. Indeed, increasing the thickness of ITO layer would result a decrease in $R_{□}$ but make it more difficult to realize complete HTM filling. In order to obtain a high efficiency of the bifacial transparent mesoscopic solid-state DSSCs, the thickness of ITO-CE has been optimized to get a compromise between $R_{□}$ and pore filling of HTM. Herein, electrochemical impendence measurement (EIS) was carried out with the solid-state DSSCs based on ITO-CEs with different thickness and their Nyquist plot and the equivalent circuit are presented in **Figure 3**. We marked the solid-state DSSCs based on ITO-CEs with the thickness of 1.1 um, 2.1 um, 3.1 um and 4.0 um as S1, S2, S3 and S4, respectively. The semicircle in low frequency region represents the R_{rec} at Spiro-OMeTAD/TiO_2 interface. At the high frequency region, the expected feature for a diffusion process is a Warburg circuit, consisting of a straight line, which closes into an arc. [22, 23] Usually, only an incomplete arc is obtained. In the present case, it is more convenient to simplify the model of such feature to a parallel R-C sub-circuit.[23] With this equivalent circuit as the insert of **Figure 3**, the characteristic parameters are obtained from the impedance spectra of the solid-state DSSCs with different thickness of ITO-CEs and summarized in **Table 1**. Clearly, with the increase of the ITO layer from 1.1 um to 3.1 um, the R_s calculated from the Z-view software has a big reduction from 755 to 216 Ω·cm^2, which mainly attribute to the decrease of the $R_{□}$ caused by the increased thickness of ITO mesoscopic layer. However, when further increasing the thickness of the ITO mesoscopic layers to 4.0 um, the R_s presents a slight increase to 287Ω·cm^2, which may be expounded by the poor filling of HTM in the high-thickness mesoscopic films leading to a slight decrease in the conductivity. However, when the ITO layer increase from 1.1 um to 4.0 um, both of the charge transfer resistance R_{ct} and the recombination resistance R_{rec} present a persistent decline, which means that charge transfer is more quickly at the interface of Spiro-OMeTAD HTM/ITO layer and the recombination of electrons and holes couples happened at the interface of TiO_2/Dye/Spiro-OMeTAD is higher at the thicker ITO-CE. Indeed, the reduced R_{ct} could be attributed to the decreased $R_{□}$ of ITO-CE and much larger contact area between Spiro-OMeTAD and ITO mesoscopic layer owing to the increased thickness of ITO-CE. However, as the rising of thickness of the ITO-CE, the pore filling of spiro-OMeTAD in multi-mesoscopic films becomes more difficult because of the deeper channels in the device, which lead to poor conduct of spiro-OMeTAD in the mesoscopic film and higher recombination of electrons and holes couples at the interface of TiO_2/Dye/Spiro-OMeTAD.

The photocurrent density-voltage (*J-V*) characteristics of solid-state DSSCs based ITO-CEs with different thickness are presented in **Figure 4**. Obviously, when the thickness of ITO-CE increases from 1.1 to 4.0 um, the open-circuit photovoltaic (V_{oc}) of the devices present a slight decrease from 0.80V to

0.77V. But, obvious changes are observed in the short-circuit photocurrent density (J_{sc}). Compared with the other three devices, device S1 shows the smallest J_{sc} of 3.42 mA·cm^{-2}, which may be caused by the largest series resistance about 755Ω·cm^2. In contrast, the devices of S2, S3 and S4 show similar J_{sc} of 4.70, 4.56 and 4.58 mA·cm^{-2} respectively, where similar series resistance of 227, 216, 287Ω·cm^2 was obtained for these devices. As the thickness of the ITO-CEs increases from 1.1 um to 2.1 um, the fill factor has a significant increase from 0.40 to 0.46, which can be interpreted by the decrease of the series resistances. However, when the thickness further increases from 2.1 um to 4.0 um, the *FF* has reduced to 0.35, which is agree well with the results of EIS and could be attributed to the poor pore filling and high recombination of electrons and holes at TiO_2/Dye/Spiro-OMeTAD interface[24-27] for the thicker channels. As a result, the optimized efficiency of the solid-state DSSC with 2.1 um ITO-CE is 1.73% under AM 1.5G irradiation.

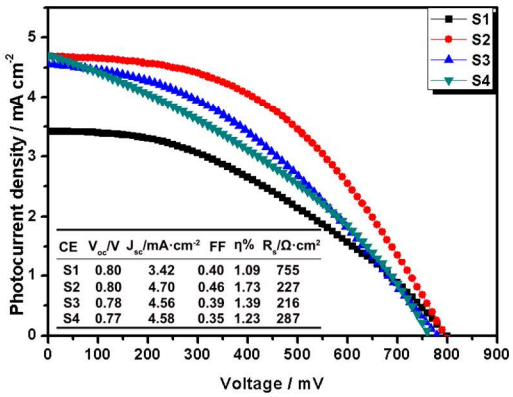

Figure 4 Photocurrent density versus applied potential curves of the solid-state DSSCs based on ITO-CEs with different thickness, where the thicknesses of TiO_2 layer and ZrO_2 layer were 2.2 um and 1.5 um respectively.

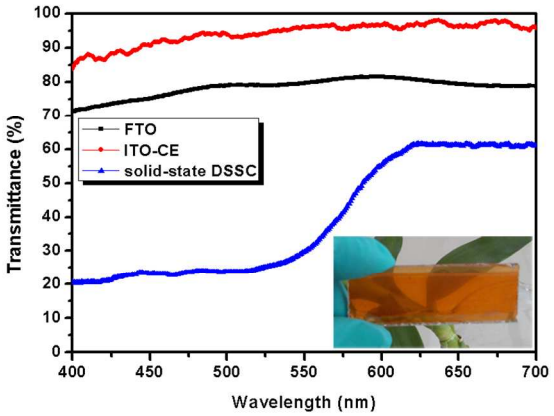

Figure 5 The Optical transmittance spectra of FTO glass, the ITO-CE and the solid-state DSSC.

Indeed, the solid-state DSSC with ITO-CE presents high transparent as shown in insert of **Figure 5**. In order to investigate the optical characterization of ITO-CE, an ultraviolet-visible spectroscopy was used to detect the transmittance of FTO glass, ITO-CE and solid-state DSSC based on ITO-CE and presented in **Figure 5**. Above 400nm, the ITO-CE led to transmittance over 83%. However, the transmittance of device solid-state DSSC sharply decreases to about 30% as the wavelength decreases to 550nm and further decreased to 20% at 400nm, which could be attributed to the absorption of the D102 and Spiro-OMeTAD.

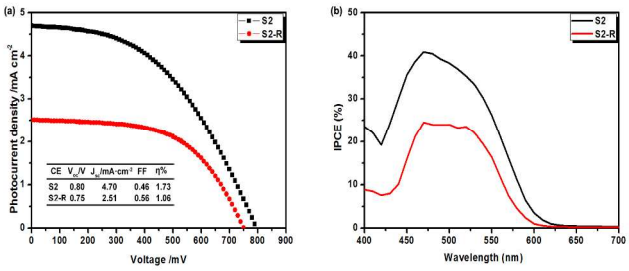

Figure 6 a) Photocurrent density versus applied potential curves of the device illumination from the front side (S2) and rear side (S2-R) respectively; b) The normalized incident-photon-to-electron conversion efficiencies (IPCE) spectra.

Figure 6a shows the *J–V* curves of the optimized monolithic solid-state DSSC S2 from the front and rear side under AM1.5 illumination with the intensity of 100 mW·cm^{-2}. Clearly, the device S2 irradiated from front side shows V_{oc} of 0.80V, J_{sc} of 4.70 mA·cm^{-2}, *FF* of 0.46, and an efficiency of 1.73%. However, when irradiated from the rear side, its curve (S2-R) exhibits an efficiency of 1.06%, approached 61% of that irradiated from front side. Note that the main reason for the efficiency loss is in J_{sc}, which is decreased to 2.51mA·cm^{-2} and about 47% loss compared to S2. This different in J_{sc} could also be observed in the incident photon-to-electron conversion efficiency (*IPCE*), which defined as the number of charge carriers collected per incident photon. **Figure 6b** presents *IPCE* spectra corresponding to the front and rear illumination of S2. It could be found that the *IPCE* spectrum of device under the rear illumination of S2-R is lower than that of device under the front illumination of S2 from 400nm to 625nm, which is agreed well with the result of J_{sc} in S2 and S2-R. Indeed, when the light is irradiated from rear side, it needs to firstly pass through Spiro-OMeTAD capping layer, ITO layer and ZrO_2 layer in this multi-hybrid junction of the device. Though the ITO-CE presents high transparency, Spiro-OMeTAD radical cations could absorb light that competes with light harvesting of dye molecules and decrease effective light absorption. In addition, it was found that the charge transport in TiO_2 film is the limiting process rather than hole transport in HTM.[28] Therefore, irradiation from rear side will form a charge distribution profile having more photo-generated charges far away from the FTO and suffer from collection losses due to longer transport distance through TiO_2 film.[19] Interested, the V_{oc} of S2 is about 0.05V higher than S2-R irradiated from ITO-CE side. The V_{oc}

could be considered as a result in the interfacial kinetics between injected electrons with back transfer electrons. Under open-circuit conditions, the rate of injected electrons from dyes is balanced with that of back transfer electrons from TiO_2 to Spiro-OMeTAD or dyes. Assuming dye regeneration is efficient, recombination from TiO_2 to dye is negligible and thus V_{oc} is given by J. Bisquert et al. [29] and L. M. Peter [30, 31] as follows:

$$V_{oc} = \frac{kT}{q} \ln\left(\frac{J_{sc}\tau_0}{q\alpha n_0}\right)$$

Where k is Boltzmann's constant, T is the temperature, q is electronic charge, τ_0 is an electron life time, α is the ratio of surface electrons concentration participated in recombination to electrons in the TiO_2 and n_0 is the electron concentration in the conduction band in the dark. Obviously, the higher J_{sc} irradiated from the front side than that irradiated from the rear side maybe account for higher V_{oc}.

Conclusions

We firstly report a bifacial transparent monolithic solid-state DSSC based on mesoscopic ITO-CE. The key trilamellar films of mesoscopic TiO_2 photoanode, ZrO_2 insulating layer and ITO-CE could be full screen-printed layer by layer, where the mesoscopic transparent conduct ITO film present low resistivity of 0.247Ω·cm. Under a standard simulated sunlight condition (AM 1.5, 100mW/cm^2), efficiency of 1.73% from the front of the solid-state DSSC and an efficiency of 1.06% from the rear side of the device are obtained respectively. This very simple and full printable transparent monolithic solid-state DSSC presents extensive application prospect such as BIPV. Higher efficient printable monolithic solid-state DSSC could be expected with better conductivity and work function CE.

Acknowledgements

The authors acknowledge the financial support from the Ministry of Science and Technology of China (863, No. SS2013AA50303), the National Natural Science Foundation of China (Grant No. 61106056), the Science and Technology Department of Hubei Province (No. 2013BAA090) and the Fundamental Research Funds for the Central Universities (HUSTNY022). We thank the Analytical and Testing Center of Huazhong University of Science and Technology (HUST) for field emission scanning electron microscopy (FE-SEM), transmission electron microscopy (TEM) and X-ray diffraction (XRD) testing.

Notes and references

Michael Grätzel Center for Mesoscopic Solar Cells, Wuhan National Laboratory for Optoelectronics, School of Optical and Electronic Information, Huazhong University of Science and Technology, Wuhan, Hubei, P. R. China, 430074. E-mail: hongwei.han@mail.hust.edu.cn; Tel: +86 27 8779 3027

Electronic Supplementary Information (ESI) available: [XRD pattern of ITO nanoparticles; Cross-sectional SEM image of the bifacial transparent solid-state DSSC based on ITO-CE]. See DOI: 10.1039/b000000x/

1. L. M. Peter, *J. Phys. Chem. Lett.*, 2011, **2**, 1861-1867.
2. M. Grätzel, R. A. Janssen, D. B. Mitzi and E. H. Sargent, *Nature*, 2012, **488**, 304-312.
3. M. Grätzel and Brian O'Regan, *Nature*, 1991, **353**, 737.
4. X. Wang, L. J. Zhi and K. Mullen, *Nano lett.*, 2008, **8**, 323-327.
5. L. Kavan, J. H. Yum and M. Grätzel, *Acs Nano*, 2011, **5**, 165-172.
6. W. Hong, Y. Xu, G. Lu, C. Li and G. Shi, *Electrochem. Commun.*, 2008, **10**, 1555-1558.
7. Z. Ku, X. Li, G. Liu, H. Wang, Y. Rong, M. Xu, L. Liu, M. Hu, Y. Yang and H. W. Han, *J. Mater. Chem. A*, 2013, **1**, 237.
8. Q. D. Tai, B. L. Chen, F. Guo, S. Xu, H. Hu, B. Sebo and X. Z. Zhao, *Acs Nano*, 2011, **5**, 3795-3799.
9. X. Li, Z. Ku, Y. Rong, G. Liu, L. Liu, T. Liu, M. Hu, Y. Yang, H. Wang, M. Xu, P. Xiang and H. W. Han, *Phys. chem. chem. phys.*, 2012, **14**, 14383-14390.
10. U. Bach, K. De Cloedt, H. Spreitzer and M. Grätzel, *Adv. Mater.*, 2000, **12**, 1060-1063.
11. U. Bach, D. Lupo, P. Comte, J. E. Moser, F. Weissortel, J. Salbeck, H. Spreitzer and M. Grätzel, *Nature*, 1998, **395**, 583-585.
12. Y. Saito, T. Kitamura, Y. Wada and S. Yanagida, *Syn. Met.*, 2002, **131**, 185-187.
13. Q. B. Meng, K. Takahashi, X. T. Zhang, I. Sutanto, T. N. Rao, O. Sato, A. Fujishima, H. Watanabe, T. Nakamori and M. Uragami, *Langmuir*, 2003, **19**, 3572-3574.
14. I. Chung, B. Lee, J. He, R. P. Chang and M. G. Kanatzidis, *Nature*, 2012, **485**, 486-489.
15. M. Xu, G. Liu, X. Li, H. Wang, Y. Rong, Z. Ku, M. Hu, Y. Yang, L. Liu, T. Liu, J. Chen and H. W. Han, *Org. Electron.*, 2013, **14**, 628-634.
16. G. K. Mor, K. Shankar, M. Paulose, O. K. Varghese and C. A. Grimes, *Nano lett.*, 2006, **6**, 215-218.
17. T. N. Murakami, S. Ito, Q. Wang, M. K. Nazeeruddin, T. Bessho, I. Cesar, P. Liska, R. Humphry-Baker, P. Comte and P. Péchy, *J. Electrochem. Soc.*, 2006, **153**, A2255-A2261.
18. J. D. Roy-Mayhew, D. J. Bozym, C. Punckt and I. A. Aksay, *Acs Nano*, 2010, **4**, 6203-6211.
19. Y. F. Chiang, C. H. Tsai, P. Chen and T. F. Guo, *Solar Energy*, 2012, **86**, 1967-1972.
20. T. Sasaki, Y. Endo, M. Nakaya, K. Kanie, A. Nagatomi, K. Tanoue, R. Nakamura and A. Muramatsu, *J. Mater. Chem.*, 2010, **20**, 8153.
21. H. Wang, G. Liu, X. Li, P. Xiang, Z. Ku, Y. Rong, M. Xu, L. Liu, M. Hu, Y. Yang and H. W. Han, *Energy Environ. Sci.*, 2011, **4**, 2025.
22. J. Bisquert, *J. Phys. Chem. B*, 2002, 325-333.
23. P. P. Boix, G. Larramona, A. Jacob, B. Delatouche, I. Mora-Seró and J. Bisquert, *J. Phys. Chem. C*, 2012, **116**, 1579-1587.
24. I. K. Ding, N. Tétreault, J. Brillet, B. E. Hardin, E. H. Smith, S. J. Rosenthal, F. Sauvage, M. Grätzel and M. D. McGehee, *Adv. Funct. Mater.*, 2009, **19**, 2431-2436.
25. H. J. Snaith, R. Humphry-Baker, P. Chen, I. Cesar, S. M. Zakeeruddin and M. Gratzel, *Nanotechnology*, 2008, **19**, 424003.
26. L. Schmidt-Mende and M. Grätzel, *Thin Solid Films*, 2006, **500**, 296-301.
27. J. Melas-Kyriazi, I. K. Ding, A. Marchioro, A. Punzi, B. E. Hardin, G. F. Burkhard, N. Tétreault, M. Grätzel, J.-E. Moser and M. D. McGehee, *Adv. Energy Mater.*, 2011, **1**, 407-414.
28. H. J. Snaith and M. Grätzel, *Adv. Mater.*, 2007, **19**, 3643-3647.
29. J. Bisquert, D. Cahen, G. Hodes, S. Rühle and A. Zaban, *J. Phys. Chem. B*, 2004, **108**, 8106-8118.
30. L. M. Peter, *Phys. chem. chem. phys.*, 2007, **9**, 2630-2642.
31. L. Peter, *J. Phys. Chem. C*, 2007, **111**, 6601-6612.